We are IntechOpen, the world's leading publisher of Open Access books Built by scientists, for scientists

4,800
Open access books available

122,000
International authors and editors

135M
Downloads

Our authors are among the

154
Countries delivered to

TOP 1%
most cited scientists

12.2%
Contributors from top 500 universities

CLARIVATE ANALYTICS BOOK CITATION INDEX INDEXED

WEB OF SCIENCE™

Selection of our books indexed in the Book Citation Index in Web of Science™ Core Collection (BKCI)

Interested in publishing with us?
Contact book.department@intechopen.com

Numbers displayed above are based on latest data collected.
For more information visit www.intechopen.com

2

Linear and nonlinear optical properties of aligned elongated silver nanoparticles embedded in silica

Raul Rangel-Rojo[1], J.A. Reyes-Esqueda[2], C. Torres-Torres[3], A. Oliver[2], L. Rodríguez-Fernandez[2], A. Crespo-Sosa[2], J.C. Cheang-Wong[2], J. McCarthy[4], H.T. Bookey[4] and A.K. Kar[4]

[1]*Departamento de Optica, Centro de Investigación Científica y de Educación Superior de Ensenada, Apartado Postal 2732, Ensenada BC 22860, México.*

[2]*Instituto de Física, Universidad Nacional Autónoma de México, Circuito de la Investigación Científica S/N, Ciudad Universitaria, Distrito Federal, México.*

[3]*Sección de Estudios de Posgrado e Investigación ESIME-Zacatenco, Instituto Politécnico Nacional, México, D.F. 07738, Mexico*

[4]*School of Engineering and Physical Sciences, David Brewster Building, Heriot-Watt University, Edinburgh, EH14 4AS, Scotland UK.*

1. Introduction

Nanoestructured materials have attracted a considerable amount of attention in the past few years for their potential use in different applications, especially in the field of optics. Because of this, the optical properties of semiconductor (Yildirim and Bulutay, 2008), organic (Kasai *et al*, 1992), and metallic nanoparticles embedded in different media, have been thoroughly studied. For metallic nanoparticles in particular, this has been driven by the possibility of the use of their nonlinear optical properties in information processing applications, and more recently for the potential implementation of plasmonic circuitry (Barnes *et al*, 2003; Maier *et al*, 2003). Regarding their nonlinear optical properties, metallic nanoparticles embedded in dielectric matrices have shown considerably large nonlinearities with response times in the picosecond regime (Inouye *et al*, 2000). One of the most important features of this class of materials is the possibility of tuning their optical properties by manipulation of the particle size, shape, and the appropriate choice of the host matrix, which has been explored to a certain extent. There are however few reports of the generation of elongated nanoparticles, and even fewer reports of the study of their linear and nonlinear optical properties (Kyoung & Lee, 1999; Elim *et al*, 2006; Ruda & Shirk, 2007; Lamarre *et al*, 2008).

Among the many techniques employed to generate nanoparticles, metal ion implantation in glass substrates has proven to be a reliable technique for producing samples with well controlled characteristics. Recently, further high energy ion irradiation with different ions, has been shown to produce highly elongated metallic nanoparticles, with a prolate spheroidal shape (Oliver *et al*, 2006). Although the position of the nanoparticles produced

through this technique is random, the resulting spheroids are aligned in the direction of incidence of the second set of ions. For such a composite with aligned particles, a strong birrefringence of the linear and nonlinear optical properties can be expected.
In this work we present a novel technique for producing elongated silver nanoparticles embedded in a silica matrix, that are aligned in a preferential direction. This is achieved through a two-step ion implantation technique, and we present high resolution electron microscopy studies of the morphology of the resulting nanoparticles. We also present a characterization of the linear and nonlinear optical properties of these materials. The nanoparticles do not form an ordered array, but because they are elongated in a preferential direction, the composite is highly anisotropic. A complete study of the anisotropy is presented, and absorption spectra results show that the usual surface plasmon resonance found in these composite materials is split into two distinct bands, due to the elongation of the nanoparticles. A correlation between the observed position of the bands and the morphology of the particles is presented.
Regarding the nonlinear response of the material, the resonant nonlinear response to femtosecond and picosecond pulses is probed, employing the z-scan technique in the former case, and a vectorial four-wave mixing technique, in the latter. The observed response consists mainly of saturable absorption, which is shown to be also highly anisotropic. An analysis of the nonlinear response obtained as function of the polarization of the light employed is made, and the results are explained based on a simple model in the case of femtosecond pulses. For the picoseconds case, we discuss some insights about the influence of the hot-electrons on the nonlinear response.

2. Sample preparation and structural characterization

Elongated silver nanoparticles were synthesized through a double ion implantation process. In the first step 2-MeV Ag^{2+} ions are implanted into host matrices consisting of high –purity silica glass plates (20×20×1 mm^3) from NSG ED-C (Nippon silica glass), at room temperature. The impurity content of the silica plates was not greater than 1 ppm, with less than 1 ppm of OH, and a total impurity content of less than 200 ppm. The samples were then thermally annealed at 600^o C in a 50%N_2+ 50% H_2 reducing atmosphere. The Ag-ion fluence and projected range, measured by Rutherford backscattering spectrometry (RBS) were 5 × 10^{16} Ag/cm^2 and 0.9 μm, respectively. Both the ion implantation process and the RBS analysis were performed at the 3 MV Tandem accelerator (NEC 9SDH-2 Pelletron) at UNAM. Optical absorption spectra of these samples showed that the result of this process was a film containing spherical-like silver nanoparticles, of around 6 nm in diameter.
Afterwards, the samples were cut into several pieces, and in order to induce deformation of the particles, each piece was irradiated at room temperature with 8 MeV Si ions at an angle of 45^o with respect to the sample surface, with Si ion fluence values in the 0.1-2.3 × 10^{16} Si/cm^2 range. According to previous results (Cheang-Wong *et al* 2006) concerning the ion beam-induced deformation of silica particles, 8 MeV Si ions were chosen because their electronic stopping power for SiO_2 is 200 times larger than the nuclear one. On the other hand, the ion projected range for this energy is 4.3 μm in SiO_2, i.e. far beyond the location of the Ag nanoparticles. The result of the second ion implantation process was elongated nanoparticles aligned in the direction of the second ion implantation.

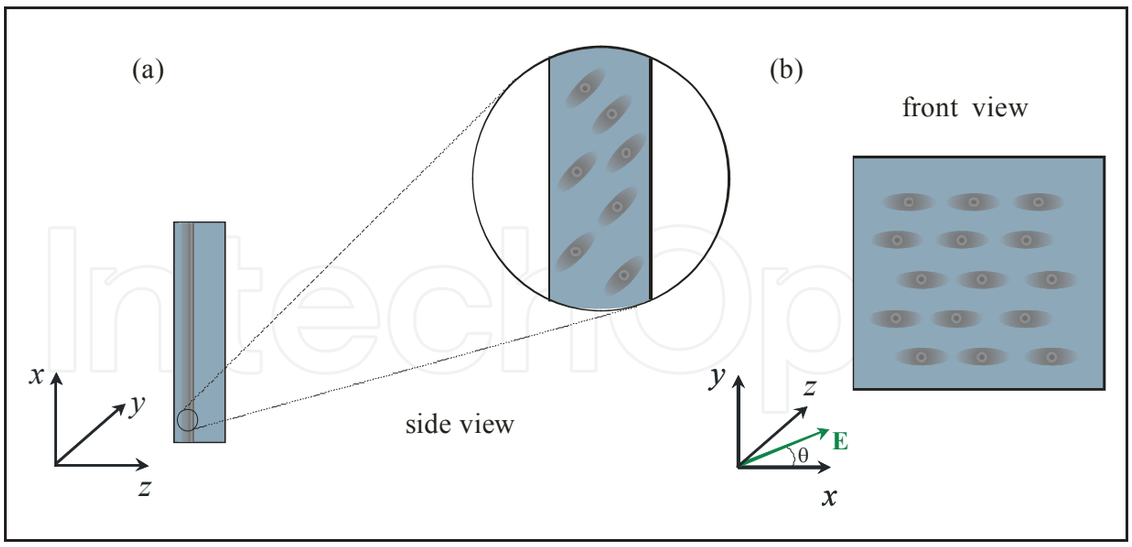

Fig. 1. Sample morphology, the side view in (a) shows the thin layer containing the elongated nanoparticles, which are aligned at 45^o with respect to the normal to the surface, and (b) the front view showing the projection of the nanoparticles and the geometry chosen for the polarization of the incident light.

The resulting sample has a 0.5 μm thick layer containing the elongated nanoparticles, at a 1 μm depth inside the silica matrix, as shown schematically in fig. 1. The particles are aligned at 45^o with respect to the substrate normal, as is also shown in fig. 1, and when viewed from the front, the projection of the nanoparticles long axes point in the direction we label as x. Evidence of the shape of the individual nanoparticles is obtained through HRTEM images of the sample, obtained with a 200 KV JEOL-2010FEG microscope in contrast-Z mode. Fig. 2 shows images taken for a sample with a 2.3×10^{16} Si/cm^2 fluence, where it can be seen that the randomly placed nanoparticles are aligned in the same direction, and that they are shaped as prolate spheroids, with an average minor axis diameter of 5 nm, and an aspect ratio of 1.7. The size distribution of the implanted sample was obtained from a digitized amplified micrograph by measuring the diameter of each nanoparticle. The size distribution obtained from the statistics over 290 measurements shows a diameter distribution centred at 5.9 nm with a standard deviation of 1.1 nm.

3. Linear optical properties. Anisotropic absorption and birrefringence

In order to characterize the linear optical properties of the samples produced by this double implantation technique, studies of the polarization dependence of the absorption spectrum were conducted, together with studies of the possible birefringence exhibited by the material.

3.1 Polarization dependent absorption spectra

An Ocean Optics Dual Channel SD2000 UV-visible spectrophotometer was used to collect the optical absorption spectra, using linearly polarized light with different polarization orientations. At the beginning, the absorption spectra had a constant 'baseline' which was attributed to the presence of a superficial layer of carbon that deposited on top of the sample

in the implantation process. This layer was removed by further baking the samples at 400° C for 5 hours. Fig. 3 shows the absorption spectra of the sample after this process, recorded at normal incidence and using two mutually orthogonal polarizations, at *0º* and *90º* which are roughly parallel (labeled $E_{\|}$), and perpendicular (labeled $E_{\perp}$) to the long axis of the nanoparticles respectively. Two different absorption bands are clearly discerned from the spectra, one centered at *365 nm* for the spectrum taken with the $E_{\perp}$ polarization, and a broader one at 517 nm for the $E_{\|}$ polarization.

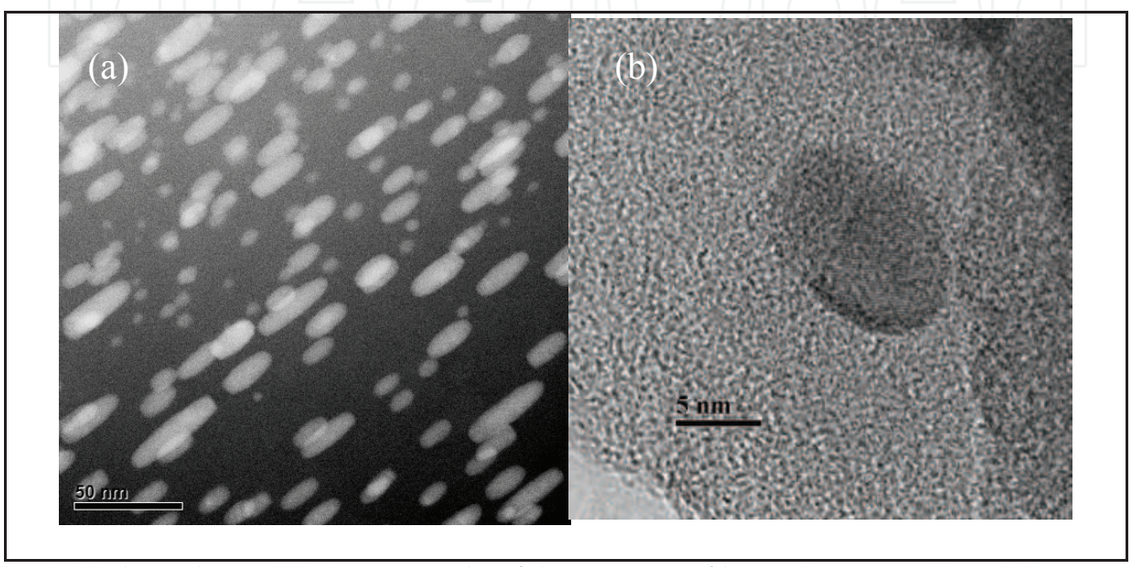

Fig. 2. High resolution TEM micrographs of the composite film: a) Z contrast (HAADF) image showing the Ag nanoparticles deformed by Si ion irradiation, obtained with a TEM, at 200 KV, with a point to point resolution of 0.19 nm. b) HRTEM micrograph of a deformed nanoparticle.

These peaks correspond to the different surface plasmon resonances for each polarization, as has been probed by studying the linear birrefringence of the sample (Reyes-Esqueda *et al*, 2008). From Fig. 3 it is easily seen that for the $E_{\|}$ polarization there is a remnant of the *365 nm* peak, this can be due to a residual misalignment with respect to the direction of elongation of the particles, or to a fraction of the nanoparticles remaining spherical after the second ion-implantation process.

Absorption spectra were also taken at intermediate polarization angles. Fig. 4 shows the values of the linear absorption coefficient extracted from the optical density (*OD*) measured at *527 nm* as function of the polarization angle θ (α=*OD* ln 10/*L* with *L* the thickness of the layer containing the particles, which was taken to be *0.5 μm*). This is the wavelength of the laser source employed in the z-scan measurements. For a collection of perfectly aligned anisotropic particles, the linear absorption coefficient $\alpha(\theta)$ can be written as (Boyd, 1992):

$$\alpha(\theta) = (\alpha_0 - \alpha_{\pi/2})\cos^2\theta + \alpha_{\pi/2}, \tag{1}$$

where α_0 is the linear absorption coefficient for $\theta=0^o$ ($E_{||}$ polarization), and $\alpha_{\pi/2}$ is the one corresponding for $\theta=90^o$ ($E_{\perp}$ polarization). Fig. 4 shows a fit to the experimental values of *OD* using expression (1) $\alpha_0= 2.76 \times 10^4\ cm^{-1}$, and $\alpha_{\pi/2} =5066\ cm^{-1}$. In this way, we can see that for a given wavelength, the linear absorption observed is strongly dependent on the polarization of the light. This anisotropic linear absorption is important for the characterization of the linear birefringence of the material, and for their nonlinear optical properties as well.

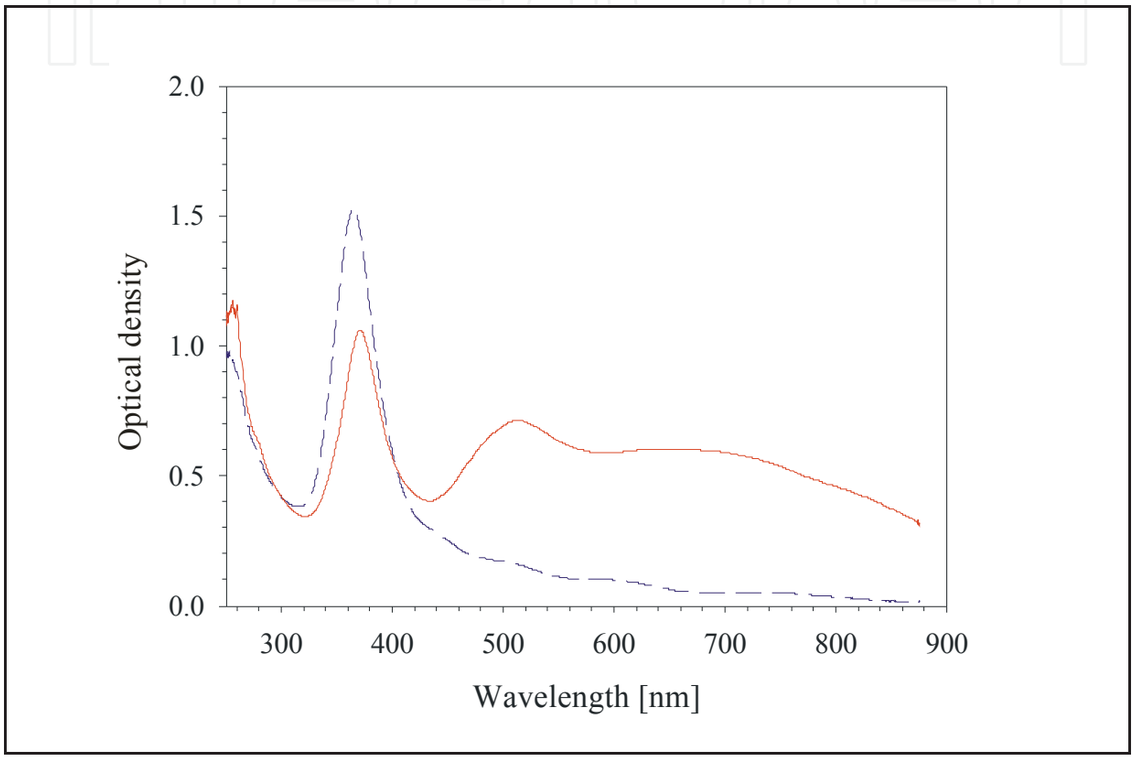

Fig. 3. Absorption spectra of the prolate spheroidal silver nanoparticle sample taken for mutually orthogonal linear polarizations, the continuous line corresponds to a polarization angle $\theta=0^o$ ($E_{||}$), and the dotted line to $\theta=90^o$ ($E_{\perp}$).

3.2 Birrefringence measurements

In order to analyze the optical anisotropy (or birefringence) of the sample, we have used an ellipsometric technique where we measure the light transmission through our samples when placed and rotated between crossed and parallel polarizers. The experimental setup shown in Fig. 5(a) was used to measure the birefringence, $\Delta n^{\alpha}=n_p(\psi)-n_s$, experienced by the probe beam when traversing the sample. The subscripts *s* and *p* in the expression refer to the linear optical eigenpolarization components for the probe beam, when traveling in the direction **k** (normal to the surface of the sample, $\hat{N}_{sample}$) at an internal angle of propagation ψ with respect to the normal of the deformed nanoparticle, $\hat{N}_{NP}$, as shown in Fig. 5(b). The corresponding refraction indices are n_s and n_p, and the superscript α refers to the angle

between the incident electric field and the *x* axis. The linearly polarized incident light may contain both linear eigenpolarizations, while the analyzer may be oriented parallel or crossed to transmit the linear polarization state parallel or orthogonal to the incident light, respectively. The complete mathematical details of the analysis for these ellipsometric measurements are given in (Gonzalez *et al,* 2008), here we only present some of the most important expressions necessary to analyze the experimental data.

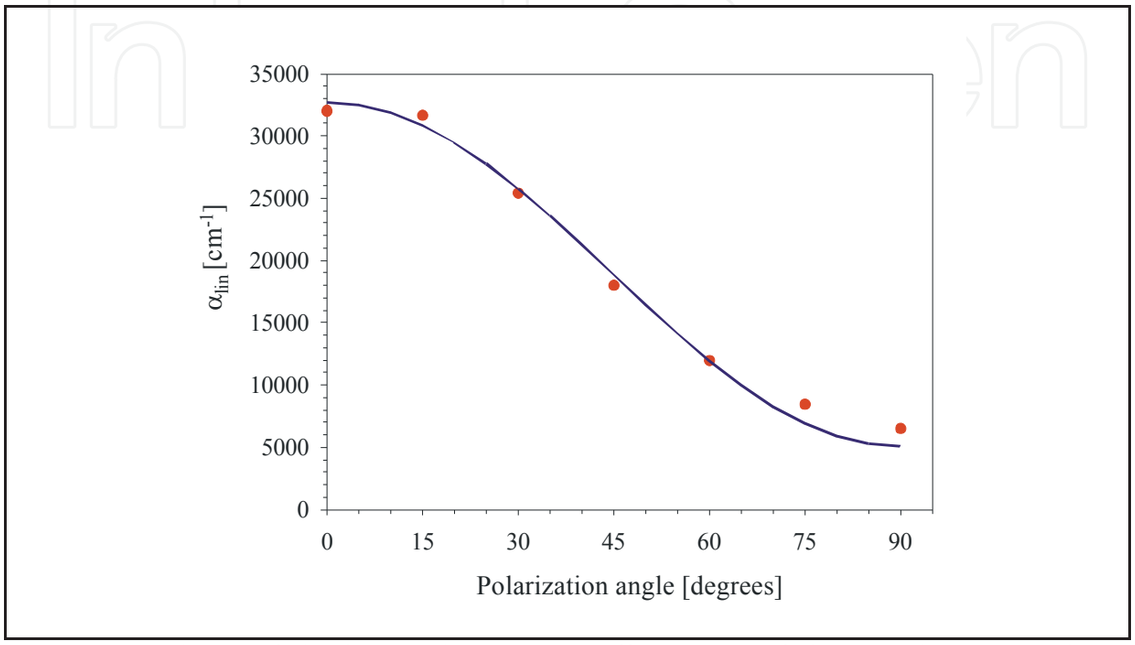

Fig. 4. Dependence of the linear absorption coefficient α_{lin} of the sample measured as a function of polarization angle θ. The dots represent the experimental points, while the line represents a fit made using expression (1).

In the coordinate system shown in Fig. 1(b), the normal to the nanoparticle can be represented by the vector

$$\hat{N}_{NP} = \begin{pmatrix} \sin\psi \\ 0 \\ \cos\psi \end{pmatrix}. \tag{2}$$

In consequence, the associated normalized eigenpolarization vectors will be [18]:

$$\hat{s} = \begin{pmatrix} 0 \\ 1 \\ 0 \end{pmatrix}, \hat{p} = \begin{pmatrix} 1 \\ 0 \\ 0 \end{pmatrix}, , \tag{3}$$

and, since the probe beam propagates parallel to the normal of the macroscopic sample, $k \parallel \hat{N}_{sample}$, which makes an angle $\psi_1=49^o$ with the normal to the nanoparticle, one can suppose that light is refracted just until it arrives to the surface of the nanoparticle according to Snell's law $sin\psi=n_{host}\ sin\psi_1/n_{NP}^{eff}$. This angle ψ_1 between both normals is the same angle between the major axis of the nanoparticle and the surface of the sample, and it is a consequence of the Si irradiation as explained further below.

On the other hand, the orientation of the incident electric field $\boldsymbol{E}_{in}$, will be determined by the polarizer orientation, which allows resolving it into the two eigenpolarization components of the optically anisotropic nanocomposite, $E_s = \hat{E}_{in} \cdot \hat{s}$, and $E_p = \hat{E}_{in} \cdot \hat{p}$, where $\hat{E}_{in} = \begin{pmatrix} \cos\alpha \\ \sin\alpha \\ 0 \end{pmatrix}$ is the unitary incident electric field and α is the angle of the polarizer (measured from *x*). Therefore, the birefringence for such a light path will be $\Delta n^{\alpha}=n_p(\psi)-n_s$, where the *p* polarization will experience a refraction index n_p, while the *s* polarization will experience n_s. In order to be able to relate it to the measured intensity, we define complex transmission factors for these two eigenpolarizations, which correspond to the transmitted electric field, as

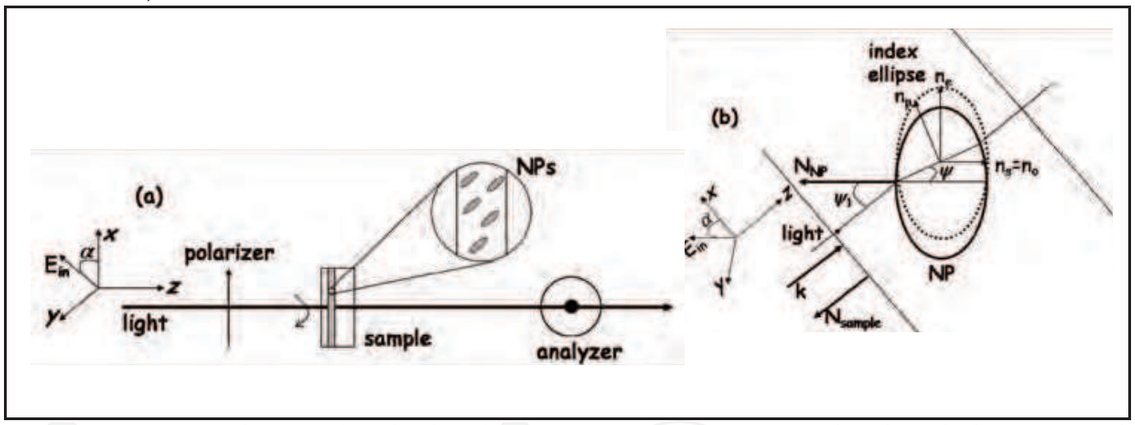

Fig. 5. Experimental setup for the birefringence measurements with white light; $\boldsymbol{E}_{in}$ stands for the incident electric field.

$$E'_s(\alpha) = A_s \exp\left(\frac{-i\pi L\Delta n^{\alpha}}{\lambda}\right)E_s\hat{s}, \text{ and } E'_p(\alpha) = A_p \exp\left(\frac{i\pi L\Delta n^{\alpha}}{\lambda}\right)E_p\hat{p}, \quad (4)$$

where A_s and A_p are the measured amplitude transmission factors for each eigenpolarization, *L* is the interaction length, *i.e.* the thickness of the NPs layer, and λ is the free-space incident wavelength. For the transmitted light, when the axes of the polarizer-analyzer system are aligned, it can be shown (Gonzalez *et al*, 2008) that the detected intensity at a given in-plane polarization α is given by

$$I(\alpha,0) = A_s{}^2 \sin^4\alpha + A_p{}^2 \sin^4\alpha + \frac{1}{2} A_s A_p \sin^2 2\alpha \cos\frac{2\pi L \Delta n^{\alpha}}{\lambda}, \tag{5}$$

while when they are crossed, the detected intensity is given by

$$I(\alpha,\frac{\pi}{2}) = \frac{1}{4}\sin^2 2\alpha \left[A_s{}^2 + A_p{}^2 - 2A_s A_p \cos\frac{2\pi L \Delta n^{\alpha}}{\lambda} \right]. \tag{6}$$

The experiment consists then of measuring these two intensities, and extracting the values of A_p^2, A_s^2, and of the birefringence of the nanocomposite from the experimental results.
We have performed the birefringence measurements at 532 and 355 nm, which are close to the surface plasmon resonances associated with the major (470 nm) and the minor (375 nm) axes of the oriented prolate-spheroid nanoparticles, as discussed above. Fig. 6 shows a typical measurement at 532 nm. For $\alpha=0$ and $\alpha=\pi/2$, we obtain A_p^2, A_s^2 respectively, from Eq. (5). On the other hand, from Eq. (6) with $\alpha=\pi/4$, we get the maximum measured birefringence as

$$\Delta n^{\max} = \frac{\lambda}{2\pi L}\cos^{-1}\left[\frac{A_s{}^2 + A_p{}^2}{2A_s A_p} - \frac{2I_{meas}{}^{\max}}{A_s A_p} \right]. \tag{7}$$

Now, given the nanoparticles geometry and their orientation, the uniaxial symmetry of the nanocomposite allows describing its refractive-index anisotropy by the ellipse shown in Fig. 5(b) with principal axes n_e and n_o, *i.e.* the extraordinary and ordinary indices, respectively. For a refracted light path at an angle ψ relative to the normal of the nanoparticles, we have $[1/n_p^2(\psi)]=\sin^2\psi/n_o^2+\cos^2\psi/n_e^2$ for the *p*-polarized light (Saleh & Teich, 1991) , whereas the *s*-polarized light sees an ordinary index n_o. Finally, the refractive-index anisotropy of the nanocomposite will be related in a first approximation to the measured birefringence by

$$n_e - n_o = \frac{\Delta n^{\max}}{\cos^2\psi} = \frac{\Delta n^{\max}}{\cos^2\left[\sin^{-1}\left(\frac{n_{host}}{n_{NP}^{eff}} \sin\psi_1 \right) \right]}. \tag{8}$$

This previous analysis has been made under the supposition that the wavelength used to perform the measurements, 532 nm, is close to the surface plasmon resonance associated with the major axis of the oriented prolate nanoparticles (at 470 nm). In such a case, it is rather clear that the index ellipse superposes with the nanoparticle as shown in Fig. 5(b). However, when exciting its minor axis, the index ellipsoid is perpendicular to the major axis of the particle. Nevertheless, the analysis is exactly the same, although the respective coordinate system (x',y',z') is rotated by $\pi/2$ around the z axis with respect to the previous one shown in Fig. 5(b). This means that the new angle α' for this last case is related to the angle α with respect to the former (x,y,z) system by $\alpha=\pi/2-\alpha'$, and since we used the same setup for both wavelengths, in order to model our results properly, we have to substitute α' for α. This substitution only affects Eq. (5), transforming it into

$$I(\alpha',0) = I(\alpha,0) = A_s{}^2 \sin^4\alpha + A_p{}^2 \sin^4\alpha + \frac{1}{2} A_s A_p \sin^2 2\alpha \cos\frac{2\pi L \Delta n^{\alpha'}}{\lambda}, \quad (9)$$

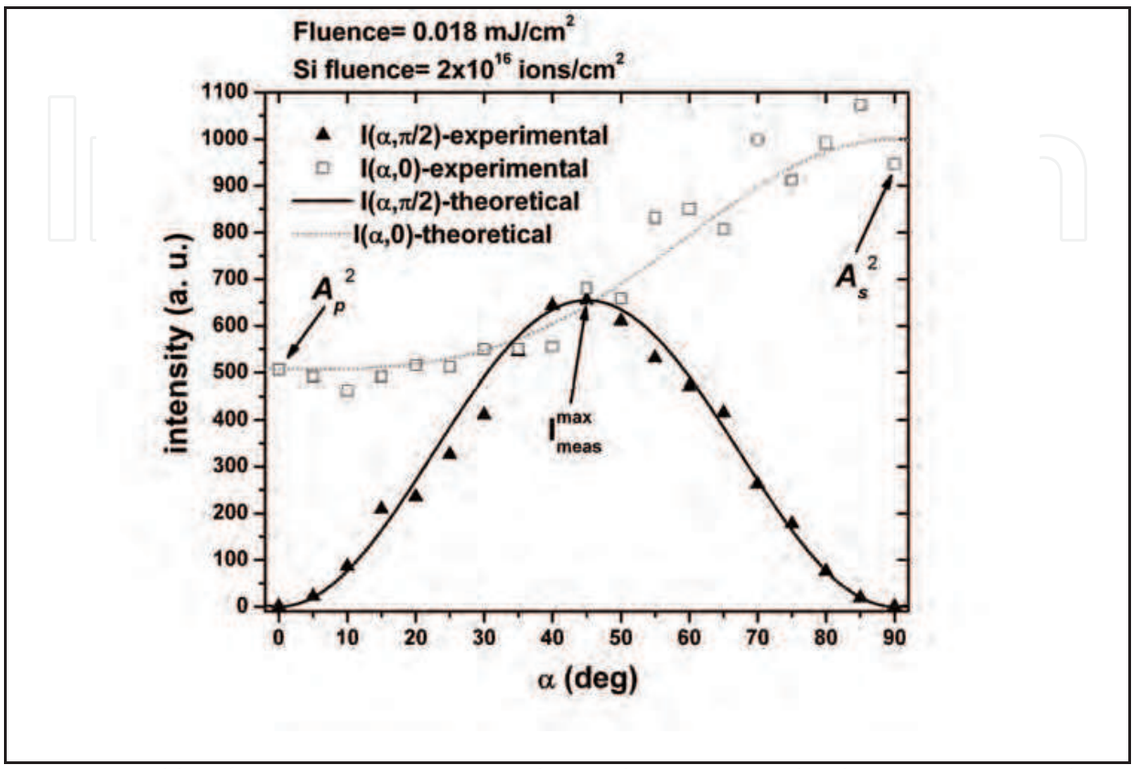

Fig. 6. Typical birefringence measurement obtained at 532 nm. The data were averaged over three consecutive measurements, taken within a given window of stability for the laser system by using a reference beam. Solid curves are the theoretical calculations given for Eqs. (5) and (6) by taking the birefringence calculated with Eq. (7).

since sin α'=cos α, cos α'=sin α , and sin 2 α'=sin 2 α. In consequence, for 355 nm, the typical measurement is a reflection of the one shown in Fig. 6 with respect to a vertical axis located at $\pi/4$. The other difference is that, now, for α =0, Eq. (9) gives $A_s{}^2$, while for $\alpha = \pi/2$, it gives $A_p{}^2$, while Δn^{max} is obtained again from Eq. (7).

Aside from the strongly polarization dependent absorption shown in section **3.1**, when placed between polarizers, there is considerable dichroism, that is, a selective absorption of one of the orthogonal components of the linear polarization of the incident beam (Saleh & Teich, 1991). By looking at Fig. 6, we can see that the perpendicular intensity is zero for α =0 and $\pi/2$, and nonzero in the middle, with a maximum at $\pi/4$. The performance of the nanocomposite is quite impressive since it is totally opaque when its optic axis is aligned with the polarizer or the analyzer, and highly transparent when is oriented at 45^o with respect to them. This optic axis corresponds to the major axis of the nanoparticle for 532 nm and to its minor axis for 355 nm. This behavior can be qualitatively understood for 532 nm as follows: when α =0 and $\alpha = \pi/2$, the transmitted electric field is crossed to the analyzer and then totally filtered. On the contrary, for α differing from these two values, only the

component of the incident electric field parallel to the major axis is absorbed, and the resulting transmitted field is not orthogonal with respect to the analyzer, obtaining a nonzero intensity measurement, which is maximum for $\alpha = \pi/4$. The same happens for 355 nm. We can quantify first this performance by looking at the extinction ratio defined as

$$\text{Extinction ratio} = 10\log_{10}\left(\frac{T_{\perp}}{T_{||}}\right) = 10\left\{abs(A_{\perp} - A_{||})\right\} \quad [dB], \tag{10}$$

which is a typical figure of merit for telecommunications. The extinction ratio for the sample with Ag nanoparticles deformed with a dose of 0.5×10^{16} *Si/cm²* is around *15 dB* for the resonance associated with the major axis of the nanoparticles and *10 dB* for the resonance associated with the minor axis, while similar values are obtained for the other samples. These values are close to 20 dB, which is a typical value at *1.55 μm*, indicating a very good performance in the visible region. For the anisotropic systems described in (Künzner *et al*, 2001; Genereux *et al*, 2001; Muskens *et al*, 2006), the corresponding extinction ratios were estimated to be around *17, 9* and *40 dB*, respectively, with corresponding thicknesses of around *100, 235* and *15 μm*, respectively.

On the other hand, by using our previous analysis, we have measured the birefringence of the anisotropic nanocomposites, where we have taken the interaction length as the FWHM of the Gaussian distribution of the implanted and deformed nanoparticles, which have a value of L=454 nm and an error of around 8%, as measured by RBS. The results are ψ_1=*49±0.5 deg*, $n_{host}=n_{SiO2}$=1.47, n_{NP}^{eff}(532nm)=$|N_{NP}$ *(532nm)*$|$=3.32, and n_{NP}^{eff}(355nm)=$|N_{NP}$ *(335nm)*$|$ =1.42, these two last values were taken from (Johnson & Christy,1972). As we have already made clear in (Oliver *et al*, 2006), the nanoparticles absorb energy through the excitation of their resonances only, and, given the size and scattered distribution of the nanoparticles into the SiO_2 matrix, radiation effects and interaction between nanoparticles (or coupling between surface plasmon resonances) are negligible.

In Table 1 we present the measured birefringence for our samples as a function of the Si fluence in the second ion implantation process, for 355 and 532 nm, as well as their refractive-index anisotropy. The aspect ratio of our deformed nanoparticles is around 1.6, which indicates a rather small shape anisotropy. However, the macroscopic birefringence of these samples is very large, as a matter of fact, practically comparable to that measured for other nanostructured semiconductor materials reported in (Künzner *et al*, 2001; Genereux *et al*, 2001; Muskens *et al*, 2006). Furthermore, when increasing the Si fluence, the nanoparticles aspect ratio increases from 1.58 to 1.69. Within the context of this paper, this means that there is an increment of their shape anisotropy, and therefore of their optical birefringence, as it is corroborated from Table 1, principally for 532 nm. This is rather difficult to see at 355 nm, since it is known that the resonance corresponding to the minor axis is less sensitive to the changes of the aspect ratio of the deformation than the resonance of the major axis. In fact, the position of this last is proportional to the aspect ratio, while the resonance of the minor axis is inversely proportional to it (Noguez, 2007). Therefore, we could expect very similar values of the birefringence measured at 355 nm for the minor axis for different values of the Si fluence. This is more evident for the highest fluence, due to the large uncertainty measured in such a case.

Si fluence [ions/cm^2]	aspect ratio	Δn^{max} (532 nm)	Δn^{max} (335 nm)	n_e-n_o (532 nm)	n_e-n_o (335 nm)
0.0	1.00	0.000	0.000	0.000	0.000
0.1	1.58	0.085±0.011	0.018±0.005	0.096±0.011	0.045±0.006
0.5	1.62	0.112±0.013	0.025±0.006	0.126±0.013	0.063±0.008
1.5	1.65	0.111±0.014	0.036±0.008	0.125±0.014	0.092±0.010
2.0	1.69	0.135±0.024	0.017±0.014	0.152±0.024	0.043±0.015

Table 1. Measured birefringence of the anisotropic silver nanoparticles with the corresponding measurement propagated uncertainties.

On the contrary, if we perform the birefringence measurements on a pure SiO_2 matrix or one with embedded spherical-like nanoparticles, no birefringence is detected. Similarly, for the deformed nanoparticles, when the wavelength used is 1064 nm, a null birefringence is detected again. These results allow us to conclude that the observed birefringence is only due to the silica embedded layer of deformed and aligned Ag nanoparticles.
Although the reported birefringence reported in (Reyes-Esqueda *et al*, 2008) is already larger than that measured in naturally anisotropic crystals (around ten times that of quartz), we believe that it can be further enhanced by controlling more precisely the morphology of the nanoparticles. Similarly, by using deformed Au or Cu nanoparticles instead of Ag, the nanocomposite would have the similar surface plasmon resonances but placed at different wavelengths, which gives other choices where to observe dichroism (Hoa *et al*, 2007). The totality of these results offers a new means of engineering highly birefringent materials on a nanoscale. These birefringent nanocomposites could be used to create a broad array of photonic integrated nanodevices, including waveplates, polarization rotators and beamsplitters; since they are very thin (0.5 μm) when compared to similar ones like those in (Künzner *et al*, 2001; Genereux *et al*, 2001; Muskens *et al*, 2006; Seward *et al*, 1974; Hasui *et al*, 2000; Matsuda *et al*, 2005). We can also remark that ion implantation and deformation of metallic nanoparticles allow obtaining a nanocomposite with a given organization of the nanoparticles therein and preventing their oxidation. On the other hand, chemical methods offer a wide variety of shapes and sizes of metallic nanoparticles, but organizing them into a matrix is not a trivial matter. A very ready-to-hand challenge is the combination of different methods to obtain an application tailored nanocomposite (Pérez-Juste *et al*, 2005).

4. Anisotropic nonlinear absorption with femtosecond pulses.

The nonlinear optical properties of the nano particle containing sample were probed using femtosecond pulses in the resonant regime. By using femtosecond pulses, we made sure that any thermal effects on the nonlinearity would be complete minimized (Rangel-Rojo *et al*, 2009). By going to the resonant regime, in this case with one of the surface plasmon resonances of the composite, we expect a large nonlinearity and anisotropy to be found. The z-scan technique was chosen since it is very sensitive to refractive index and absorption changes induced by light.
The light source employed in the experiments was an OPA (model Spectra Physics OPA-800) which was pumped by a regeneratively amplified Ti:Sapphire laser (Spectra Physics Spitfire) emitting 1 mJ pulses at a 800 nm wavelength with a repetition rate of 1 kHz, and a pulse width of 70 fs. The signal wavelength of the OPA was tuned to around 1290 nm, and

the idler output oscillating at 2.1 μm was quadrupled in frequency by two consecutive second harmonic crystals to yield pulses at a 527 nm wavelength. The standard open-aperture z-scan set-up was used to study the nonlinear absorption of the sample, using a lens with focal length f=20 cm to focus the 233 fs pulses at 527 nm into the sample, resulting on a beam waist w=33 μm.

Fig. 7 shows experimental results obtained for *150 nJ* pulses, and two orthogonal polarizations. The data for $\theta = 0^o$ polarization shows the signature of saturable absorption, *i.e.* increased transmittance with higher irradiance, while the one at $\theta = 90^o$ shows no discernible change, indicating a much weaker nonlinearity, that is, a higher saturation irradiance I_s for this polarization. The nonlinear absorption of the sample is thus highly anisotropic, so we make a study of the nonlinearity for different input polarization angles and pulse energies to fully characterize the response. For all the input polarizations and pulse energies studied, the open aperture results showed a saturating nonlinearity, which can be modelled by an intensity dependent absorption coefficient $\alpha(I)$ given by:

$$\alpha(I) = \frac{\alpha_{lin}}{1 + I / I_s}, \tag{11}$$

where α_{lin} is the linear absorption coefficient, and I_s is the saturation irradiance. This model nonlinear absorption corresponds for example to a two-level system near resonance.

The z-scan results were analyzed using expression (11) to calculate transmission through the sample (by solving $dI/dz' = -\alpha(I) I$, integrated from $z'=0$ to $z'=L$, the sample thickness), and the input irradiance was considered as the gaussian at each sample position z, as described in references (Rangel-Rojo *et al*, 1995; Rangel-Rojo, *et al*, 1998) for example. Fig. 8 shows the experimental results obtained for a $\theta = 0^o$ input polarization, and a pulse energy of *30 nJ*. Also shown is the fit made using the procedure previously described. The same procedure was performed with all the z-scan traces obtained at the different polarization angles employed, and using the results at the lowest pulse energies where an effect was clearly seen. We used the results for the lowest energies possible, in order to make sure that the nonlinear absorption approximates to that in expression (11) as much as possible. For high irradiance values the nonlinear absorption can deviate considerable from that of a two-level saturable absorber, as it has been shown for other materials (Rangel-Rojo *et al*, 1998).

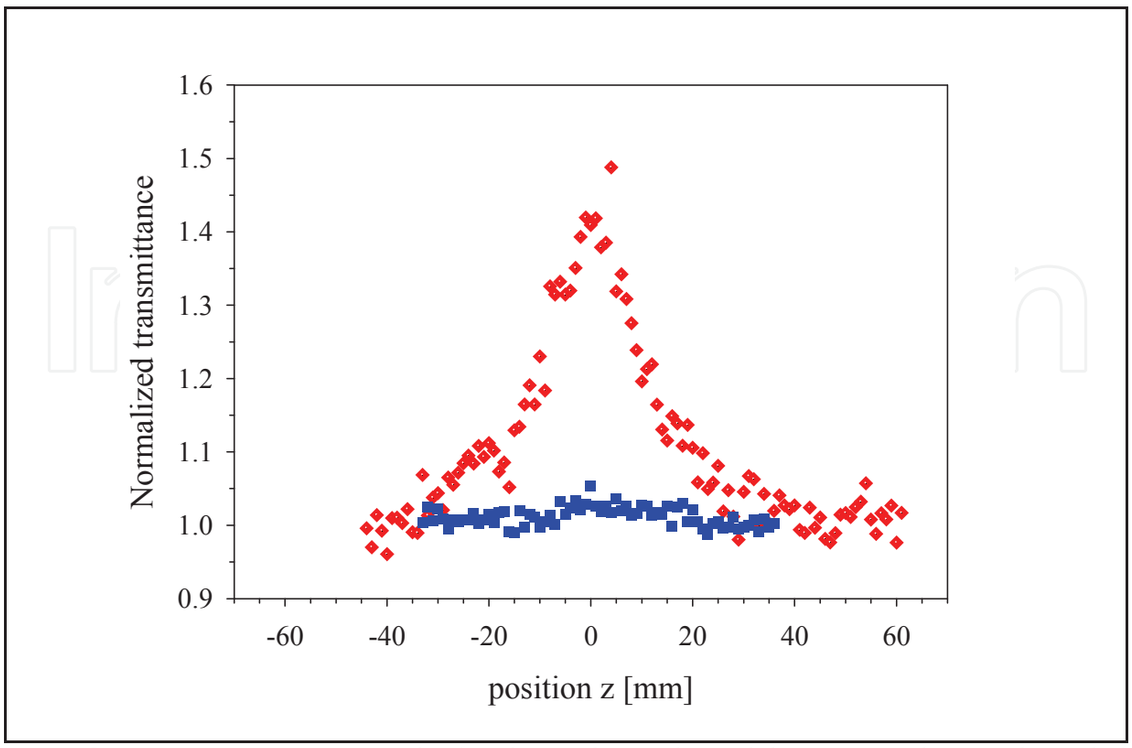

Fig. 7. Open aperture z-scan results for the prolate spheroidal nanoparticle sample with fs pulses at 527 nm. The results are shown for a pulse energy of 150 nJ, and for two different input polarizations, which are labelled $\theta = 0^o$ (diamonds), and $\theta = 90^o$ (squares).

For each input polarization angle θ, the fit to the open z-scan results yields a value for I_s. Fig. 9 shows the values of I_s extracted from the fits as a function of θ. The figure shows a rapidly growing I_s value for θ going to 90º. In fact, pulse energies as high as *300 nJ* were needed for θ =90º to actually obtain a measurable effect. In order to understand this dependence we notice that for a two-level saturable absorber, the saturation irradiance is given by:

$$I_s = \frac{\hbar\omega}{\sigma\tau} \tag{12}$$

where $\hbar\omega$ is the photon energy, σ is the absorption cross section of the transition, and τ is the lifetime of the excited state. Using the fact that the absorption coefficient can be written as $\alpha_{lin} = \sigma N$ with N the number density of the particles, together with expression (1) for $\alpha(\theta)$, we can write the polarization-angle dependent saturation irradiance $I_s(\theta)$ as:

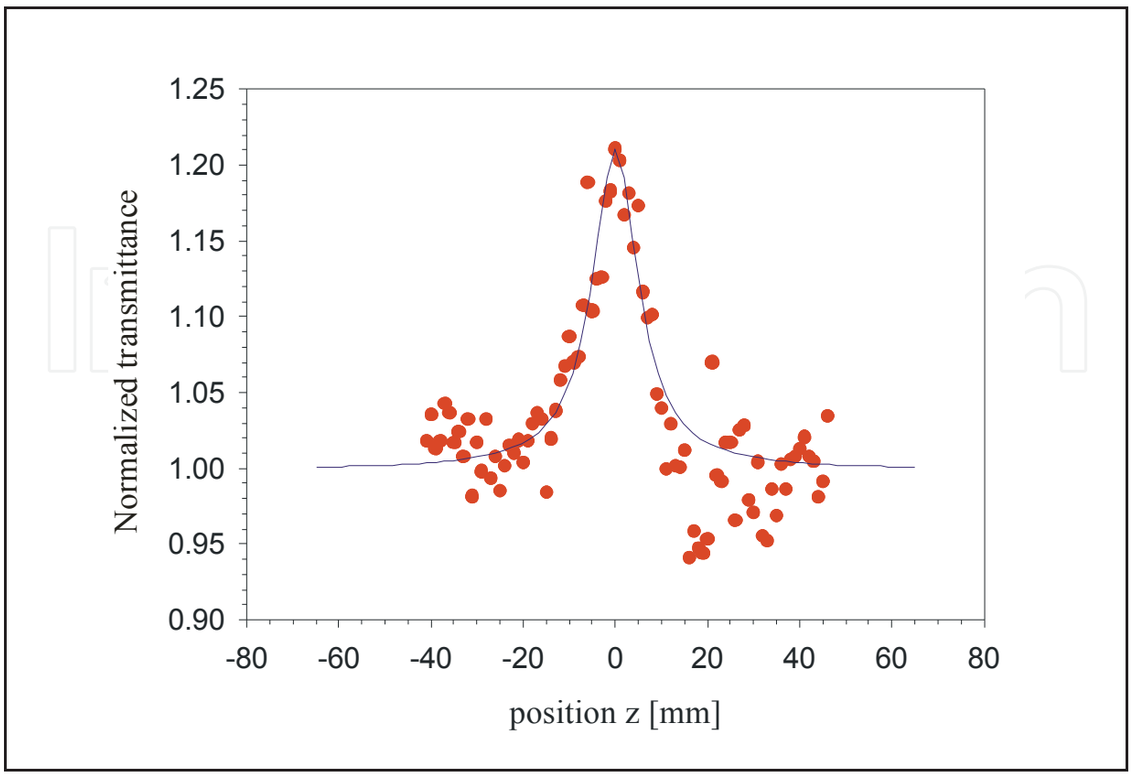

Fig. 8. Z-scan result for a $\theta=0^o$ polarization, and a pulse energy of *30 nJ*. The circles represent the experimental data, while the continuous line represents the fit made using the procedure described in the text.

$$I_s(\theta) = \frac{N\hbar\omega}{\tau[(\alpha_0 - \alpha_{\pi/2})\cos^2\theta + \alpha_{\pi/2}]}. \tag{13}$$

Fig. 9 shows the fit obtained using this expression, together with the data extracted from the z-scan results. Given the fit for α (θ) shown in Fig. 4, the only fitting parameter is the constant $N\hbar\omega/\tau$. As it can be seen from the figure, the fit reproduces the observed angle dependence of the saturation irradiance reasonably well, for a $N\hbar\omega/\tau = 9.5 \times 10^5$ *GW/cm*^{3} value. To get a better fit, it is probably necessary to consider a more realistic nonlinear absorption model, such as the three-level model described in (Rangel-Rojo *et al*, 1998).
Although a saturating nonlinearity is not strictly a third order one, for small values of I/I_s expression (11) can be approximated as:

$$\alpha(I) = \frac{\alpha_{lin}}{1 + I/I_s} \approx \alpha_{lin}\left[1 - \frac{I}{I_s}\right]. \tag{14}$$

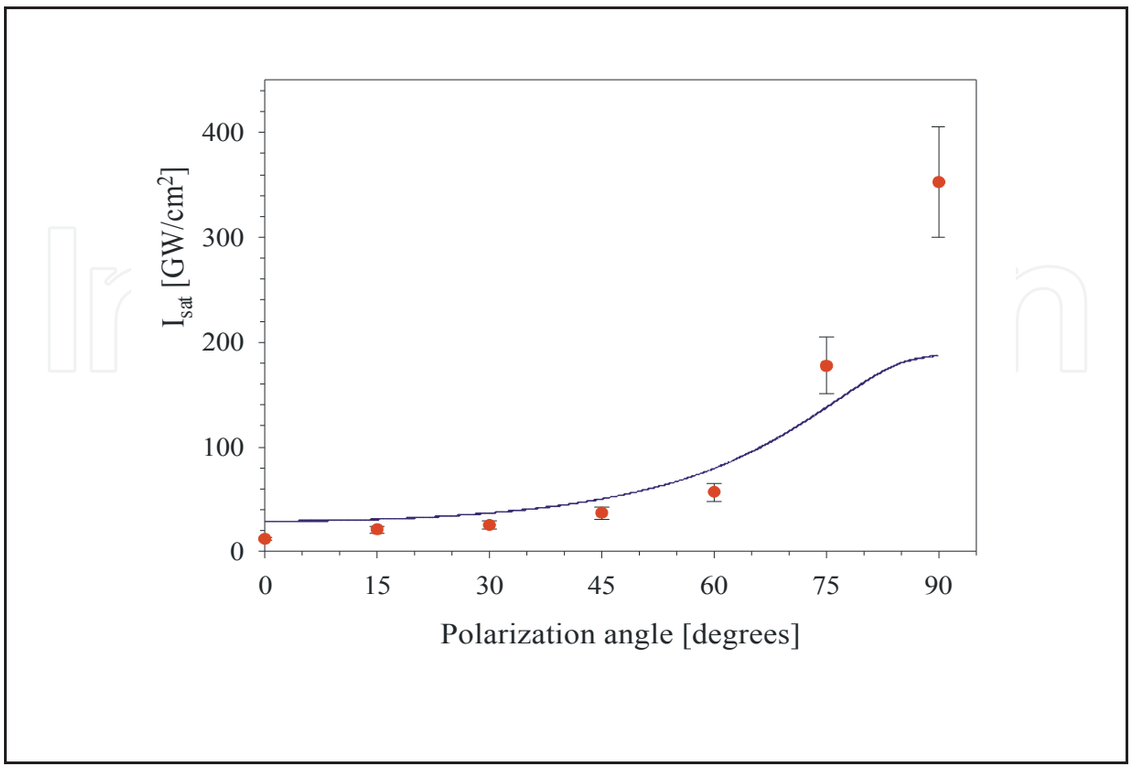

Fig. 9. Saturation irradiance extracted from the z-scan data as a function of polarization angle θ. The filled circles represent the I_s values extracted from the z-scan data, and the line represents a fit made using expression (4).

When this is compared with the usual expression for a third-order nonlinearity, $\alpha(I) = \alpha_{lin} + \beta I$, with β the two-photon absorption coefficient, we can make $\beta = -\alpha_{lin}/I_s$. Since β is related to $Im\ \chi^{(3)}$ through $Im\ \chi^{(3)} = \lambda\varepsilon_0 n_0^2 c\beta/4\pi$ (in SI units), we can use the fitted $I_s(\theta)$ values to calculate angle dependent β and $Im\ \chi^{(3)}$ values, which are contained in table 2. From the table, it can be seen that $|Im\ \chi^{(3)}|$ takes values as large as $6.55 \times 10^{-18}\ m^2/V^2$ ($4.7 \times 10^{-10}\ esu$).

θ [degrees]	α_{lin} [cm^{-1}]×10^4	I_s [GW/cm^2]	β [cm/GW]	Im $\chi^{(3)}$ [m^2/V^2]×10^{-18}
0	3.2	12.2	-2610	-6.55
15	3.16	21.0	-1510	-3.78
30	2.54	25.6	-994	-2.49
45	1.8	36.7	-489	-1.23
60	1.2	56.9	-211	-0.528
75	0.844	178	-47.5	-0.1119
90	0.648	353	-18.4	-0.046

Table 2. Fitted nonlinear optical coefficients.

We have shown results for the nonlinear absorption observed in a silica substrate containing a layer of aligned prolate spheroidal silver nanoparticles. The nonlinear absorption mechanism is saturable absorption from the broad surface plasmon resonance band, and we have found it to be highly anisotropic. We have also shown that the dependence of the

linear absorption, and saturation irradiance with the polarization angle observed, can be reasonably well explained by a simple two-level saturation model.

5. Anisotropic nonlinear response to picosecond pulses. Self-diffraction studies.

In order to see how the nonlinear response would change for longer pulse durations, we also performed nonlinear optical measurements in the picosecond regime (Rodríguez-Iglesias et al, 2009; Reyes-Esqueda et al, 2009), using for these experiments a self-diffraction technique, together with 'P-scan' measurements of the transmitted intensities as a function of the incident one. The self-diffraction technique has proven to be very sensitive for measuring absorptive and refractive index changes induced by light (Torres-Torres et al, 2009). The advantages of this technique are related to its simplicity for obtaining absorptive and refractive coefficients, and for the possibility to identify the physical mechanisms responsible of the measured nonlinear absorption and refraction at the same time (Torres-Torres et al, 2008a). The main disadvantage is that sophisticated techniques of noise elimination could be required if the nonlinear response is small (Torres-Torres et al, 2008b). Therefore, in this section, we report the use of self-diffraction and P-scan (Banerjee et al, 1998) methods at 532 nm and 26 ps, to resolve the real and the imaginary parts of the linear independent components of $\chi^{(3)}$ for the anisotropic Ag nanocomposites. For nonlinear refraction, we obtained a pure electronic and self-focusing response, while for nonlinear absorption, as in the femtosecond regime, we observed saturable absorption.

5.1 Third order nonlinear polarization for anisotropic metallic nanocomposites

Since we are dealing with anisotropic systems, it is necessary to take into consideration the full tensorial character of the nonlinear response characterized by the third order nonlinear macroscopic susceptibility tensor (Reyes-Esqueda et al, 2009). In particular, we will write the proper contributions to the third order nonlinear polarization for metallic nanocomposites showing uniaxial symmetry, when measuring by means of a totally degenerate wave mixing setup. Such an expression will put this polarization in terms of the nonzero, independent components of the macroscopic susceptibility tensor and, most importantly, in terms of the angular position of the composite.

According to (Sutherland, 1996), the third order nonlinear polarization is written in general as

$$\mathbf{P}^{(3)} = \boldsymbol{\chi}^{(3)} \vdots \mathbf{EEE}, \tag{15}$$

which can be written for each Cartesian component as

$$P_i^{(3)}(\omega_4) = 6\sum_{jkl} \chi_{ijkl}^{(3)}(-\omega_4;\omega_1,\omega_2,\omega_3) E_j(\omega_1) E_k(\omega_2) E_l(\omega_3), \tag{16}$$

where $\chi^{(3)}_{ijkl}(-\omega_4;\ \omega_1,\omega_2,\omega_3)$ is the macroscopic third order susceptibility of the material, with $\omega_4=\omega_1+\omega_2+\omega_3$, and ω_i, $i=1,2,3$, are the frequencies of the incident beams.

On the other hand, for an uniaxial system, aligned but not oriented (D_∞ symmetry) (Davis et al, 2008), the susceptibility tensor has only 11 nonzero elements, 10 of which are independent, for

completely non-degenerate wave mixing. In the case of a single degeneracy, only 8 nonzero elements remain, 7 of which are independent, but in fully degenerate wave mixing, where $\omega_1=\omega_2=\omega$, and $\omega_3=-\omega$, only 3 nonzero independent components remain, which are $\chi^{(3)}_{1111}$, $\chi^{(3)}_{1133}$, and $\chi^{(3)}_{3333}$ (Davis, et al, 2008). In consequence, the nonlinear polarization of a general uniaxial system, for the fully degenerate case, may be written as

$$P_1(\omega)=\begin{bmatrix}\chi^{(3)}_{1111}\left\{3E_1(\omega)E_1(\omega)E_1^*(\omega)+2E_1(\omega)E_2(\omega)E_2^*(\omega)+E_2(\omega)E_2(\omega)E_1^*(\omega)\right\}+\\ \chi^{(3)}_{1133}\left\{6E_1(\omega)E_3^*(\omega)+3E_3(\omega)E_1^*(\omega)\right\}E_3(\omega)\end{bmatrix};$$

$$P_2(\omega)=\begin{bmatrix}\chi^{(3)}_{1111}\left\{3E_2(\omega)E_2(\omega)E_2^*(\omega)+2E_1(\omega)E_2(\omega)E_1^*(\omega)+E_1(\omega)E_1(\omega)E_2^*(\omega)\right\}+\\ \chi^{(3)}_{1133}\left\{6E_2(\omega)E_3^*(\omega)+3E_3(\omega)E_2^*(\omega)\right\}E_3(\omega)\end{bmatrix};$$

$$P_3(\omega)=\begin{bmatrix}\chi^{(3)}_{1133}\left\{3\left(E_1(\omega)E_1(\omega)+E_2(\omega)E_2(\omega)\right)E_3^*(\omega)+6\left(E_1(\omega)E_1^*(\omega)+E_2(\omega)E_2^*(\omega)\right)E_3(\omega)\right\}+\\ 3\chi^{(3)}_{3333}E_3(\omega)E_3(\omega)E_3^*(\omega)\end{bmatrix}, \tag{17}$$

where $E_i^*(\omega)=E_i(-\omega)$, such that $E_i(\omega)E_i^*(\omega)=E_i(\omega)E_i(-\omega)=|E_i(\omega)|^2$, and $E_i(\omega)E_i(\omega)=E_i^2(\omega)$.
Now, in order to determine the components of the susceptibility tensor for an uniaxial material by using the last expression and fully degenerate wave mixing, it is necessary to choose the laboratory coordinate system such that the *z*-axis is parallel to the optical axis of the nanocomposite. However, such a coincidence it is not obvious for the anisotropic metallic nanocomposites studied in this work, since the metallic nanoparticles are embedded into a SiO_2 matrix and then deformed in the direction of a Si ion beam, becoming an uniaxial system. In consequence, the electric field of the incident light beam will always make an angle θ with this optical axis. Therefore, the most convenient way of performing the calculations is giving preference to the deformed nanoparticle coordinate system, expressing the incident electric field in this frame and then coming back to the laboratory frame. To do this in the simplest manner, one can choose the laboratory and the particle systems such that their *x*-axes coincide, the *y*-axis of the laboratory frame is parallel to the wavevector of the incident light, the electric field is parallel to the *z*-axis of the laboratory, and that this last makes an angle θ to the nanoparticle *z*-axis. This choice is shown in detail in Fig. 10.
As it was established above, Eq. (17) gives the nonlinear polarization of the whole system in its main axes; consequently, for the anisotropic metallic nanocomposite, this polarization may be expressed in the nanoparticle frame by rewriting the electric field in that system, coming back later to the laboratory frame. Thus, Eq. (17) may be written in the *xyz*-frame of the nanoparticle, as

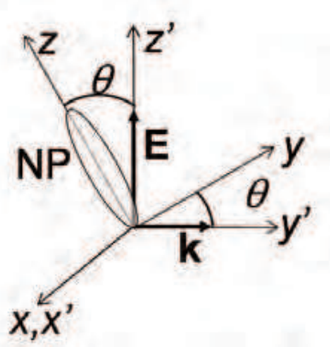

Fig. 10. Reference systems for the laboratory (primed) and the anisotropic metallic nanoparticle (unprimed).

$$\mathbf{P}_{\mathbf{NL}}^{(3)}(\omega)=\chi_{1111}^{(3)}\left[\begin{array}{l}\left\{3E_x(\omega)\left|E_x(\omega)\right|^2+2E_x(\omega)\left|E_y(\omega)\right|^2+E_y^2(\omega)E_x^*(\omega)\right\}\hat{\mathbf{i}}+\\ \left\{3E_y(\omega)\left|E_y(\omega)\right|^2+2E_y(\omega)\left|E_x(\omega)\right|^2+E_x^2(\omega)E_y^*(\omega)\right\}\hat{\mathbf{j}}\end{array}\right]+$$

$$+\chi_{1133}^{(3)}\left[\begin{array}{l}\left\{6E_y(\omega)E_z^*(\omega)+3E_z(\omega)E_y^*(\omega)\right\}E_z(\omega)\hat{\mathbf{i}}+\\ \left\{6E_x(\omega)E_z^*(\omega)+3E_z(\omega)E_x^*(\omega)\right\}E_z(\omega)\hat{\mathbf{j}}+\\ \left\{3\left(E_x^2(\omega)+E_y^2(\omega)\right)E_z^*(\omega)+6\left(\left|E_x(\omega)\right|^2+\left|E_y(\omega)\right|^2\right)E_z(\omega)\right\}\hat{\mathbf{k}}\end{array}\right]+, \tag{18}$$

$$+3\chi_{3333}^{(3)}E_z(\omega)\left|E_z(\omega)\right|^2\hat{\mathbf{k}}$$

where, by using Fig. 10, the components of the electric field can be written in such a frame as

$$\begin{aligned}&E_x(\omega)=E_x^*(\omega)=0,\\ &E_y(\omega)=E(\omega)\sin\theta\ ,\\ &E_z(\omega)=E(\omega)\cos\theta\end{aligned} \tag{19}$$

This allows rewriting the third order nonlinear polarization for the anisotropic metallic nanocomposite in terms of the angle between the electric field and the axis of the nanoparticle, which defines the optical axis of the nanocomposite, as

$$\mathbf{P}_{\mathbf{NL}}^{(3)}(\theta;\omega)=3\left|E(\omega)\right|^2E(\omega)\left[\chi_{1111}^{(3)}\sin^3\theta\hat{\mathbf{j}}+\frac{3}{2}\chi_{1133}^{(3)}\sin 2\theta\left\{\cos\theta\hat{\mathbf{j}}+\sin\theta\hat{\mathbf{k}}\right\}+\chi_{3333}^{(3)}\cos^3\theta\hat{\mathbf{k}}\right]. \tag{20}$$

When the incident electric field is parallel to the x-axis, the nonlinear polarization is trivially given by

$$\mathbf{P}_{\mathbf{NL}}^{(3)}(\omega)=\mathbf{P}_{\mathbf{NL,lab}}^{(3)}(\omega)=3\left|E(\omega)\right|^{2}E(\omega)\chi_{1111}^{(3)}\hat{\mathbf{i}}\,. \tag{21}$$

When projecting the polarization components given by Eq. (20) on the laboratory frame *y'*,*z'*, the nonlinear polarization is expressed as

$$\mathbf{P}_{\mathbf{NL,lab}}^{(3)}(\theta;\omega)=3\left|E(\omega)\right|^{2}E(\omega)\left[\chi_{1111}^{(3)}\sin^{3}\theta\left(\cos\theta\hat{\mathbf{j}}'-\sin\theta\hat{\mathbf{k}}'\right)+3\chi_{1133}^{(3)}\sin\theta\cos\theta\hat{\mathbf{j}}'+\chi_{3333}^{(3)}\cos^{3}\theta\left(\sin\theta\hat{\mathbf{j}}'+\cos\theta\hat{\mathbf{k}}'\right)\right] \tag{22}$$

.

These last two equations, Eqs. (21) and (22), apply to an uniaxial, aligned but not ordered system, in the same way that the one typically found in literature (Boyd, 1992; Sutherland, 1996):

$$\mathbf{P}_{\mathbf{NL}}^{(3)}(\omega)=6\mathbf{E}\cdot\mathbf{E}^{*}\mathbf{E}\chi_{1122}^{(3)}+3\mathbf{E}\cdot\mathbf{E}\mathbf{E}^{*}\chi_{1221}^{(3)}\,, \tag{23}$$

applies to isotropic systems. Eq. (21) determines $\chi^{(3)}_{1111}$ directly when making measurements for the incident electric field perpendicular to the major axis of the nanoparticles, but all three components are present in Eq. (22). Therefore, in order to determine each of them separately, it becomes necessary to perform at least two other measurements as a function of the angle of incidence of the light with respect to the major axis of the particles, such that we obtain enough equations to determine the other two components of the nanocomposite tensor, $\chi^{(3)}_{1133}$ and $\chi^{(3)}_{3333}$.

Nevertheless, for the type of materials in consideration, it is necessary to take into account the refraction of light at the input face of the sample. Then, the simplest way is to perform one measurement of the wave mixing signal at normal incidence and other one such that the electric field is parallel to the major axis of the nanoparticle, which can be difficult due to refraction, such that the angle between them is the smallest possible. In conclusion, one has to perform at least three measurements in order to determine the three nonzero, independent components of the third order susceptibility tensor of an anisotropic metallic nanocomposite: one measurement should be performed at normal incidence with the electric field in the same plane of the major axis of the nanoparticle, making an angle between them given by the angle of deformation of the particles by the Si ion beam (Fig. 11(a)); a second one, at normal incidence too, but the electric field parallel to the minor axis of the nanoparticles, which is achieved by rotating the sample by 90° with respect to the previous case (Fig. 11(b)); finally, a last measurement such that the electric field and the major axis of the particle are parallel, or the angle between them is the minimum allowed by refraction (Fig. 11(c)). This last measurement is achieved by rotating the sample from case (a) with respect to an axis perpendicular to the plane of Fig. 11.

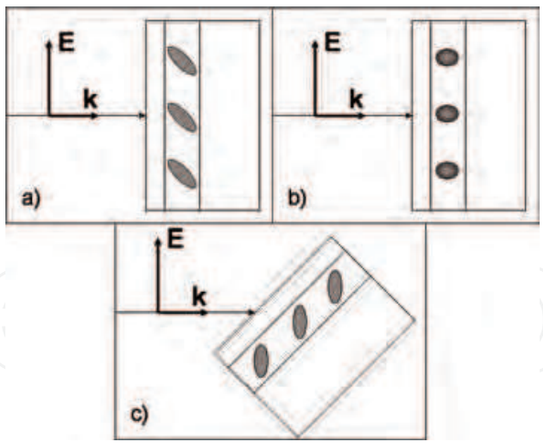

Fig. 11. Fully degenerate wave mixing measurements for anisotropic metallic nanocomposites. a) measurement at normal incidence generally implying all the three components of the tensor, b) determination of □(3)1111 at normal incidence, and c) determination, if possible due to the light refraction (not illustrated), of $\chi^{(3)}{}_{3333}$.

From what has been said above, one can rewrite Eq. (20) as

$$\mathbf{P}_{\mathbf{NL}}^{(3)}\left(\theta;\omega\right)=\left|E\left(\omega\right)\right|^{2}E\left(\omega\right)\boldsymbol{\chi}_{\mathbf{eff}}^{(3)}, \tag{24}$$

where

$$\boldsymbol{\chi}_{\mathbf{eff}}^{(3)}=3\left[\left(\chi_{1111}^{(3)}\sin^{3}\theta+\frac{3}{2}\chi_{1133}^{(3)}\sin 2\theta\cos\theta\right)\hat{\mathbf{j}}+\left(\frac{3}{2}\chi_{1133}^{(3)}\sin 2\theta\sin\theta+\chi_{3333}^{(3)}\cos^{3}\theta\right)\hat{\mathbf{k}}\right], \tag{25}$$

is the effective third order susceptibility of the nanocomposite, when measuring at a given tilt of θ between the nanoparticle and the incident electric field, after considering light refraction. This last expression allows us finally to write

$$\left|\boldsymbol{\chi}_{\mathbf{eff}}^{(3)}\right|^{2}=9\left[\begin{array}{l}\left|\chi_{1111}^{(3)}\right|^{2}\sin^{6}\theta+\left|\chi_{3333}^{(3)}\right|^{2}\cos^{6}\theta\\+\frac{3}{2}\sin^{2}2\theta\left\{\begin{array}{l}\frac{3}{2}\left|\chi_{1133}^{(3)}\right|^{2}\\+\sin^{2}\theta\left(\mathrm{Re}\,\chi_{1111}^{(3)}\,\mathrm{Re}\,\chi_{1133}^{(3)}+\mathrm{Im}\,\chi_{1111}^{(3)}\,\mathrm{Im}\,\chi_{1133}^{(3)}\right)\\+\cos^{2}\theta\left(\mathrm{Re}\,\chi_{1133}^{(3)}\,\mathrm{Re}\,\chi_{3333}^{(3)}+\mathrm{Im}\,\chi_{1133}^{(3)}\,\mathrm{Im}\,\chi_{3333}^{(3)}\right)\end{array}\right.\end{array}\right]. \tag{26}$$

In consequence, when measuring according to what has been explained for Fig. 11, cases b) and c), we would obtain $|\chi^{(3)}{}_{eff}|^2=9|\chi^{(3)}{}_{1111}|^2$, and $|\chi^{(3)}{}_{eff}|^2=9|\chi^{(3)}{}_{3333}|^2$, respectively; while for case a), we would apply Eq. (26) fully.

5.2 Nonlinear optical measurements

The third order nonlinear optical response for a thin nonlinear optical media with strong absorptive response can be obtained by identifying the vectorial self-diffraction intensities generated by two incident waves (Torres-Torres et al, 2009). In this work, we first measured the nonlinear optical absorption using a P-scan technique (Banerjee et al, 1998), and later we used these results in order to fit the experimental data obtained by scalar self-diffraction experiments. The measurements were performed at IFUNAM's Nonlinear Optics laboratory using a Nd-YAG PL2143A EKSPLA laser system at λ=532 nm with a 26 ps pulse duration (FWHM) and linear polarization. The maximum pulse energy in the experiments was 0.1 mJ, while the intensity ratio between the two beams in the self-diffraction setup was 1:1. The radius of the beam waist at the focus in the sample was measured to be 0.1 mm. The results obtained are the average of single-pulse measurements widely spaced in time, well below the ablation threshold, in order to avoid thermal effects from accumulated pulses and assure reversible and reproducible nonlinear optical effects. Both setups are schematized in Fig. 12, where RPD represents a photodetector used for monitoring the laser stability; PD1 and PD2 are photodetectors for measuring the optical transmittance of the sample, while PD3 detects the self-diffraction signal. The mirrors were placed in order to obtain the same optical path for the two incident beams. We calibrated the self-diffraction measurements using a CS_2 sample, which is a well known nonlinear optical material with $|\chi^{(3)}_{eff}|=1.9\times10^{-12}$esu (Eisaman et al, 2005). For the single beam transmittance measurement in the P-scan experiments, we blocked one of the beams in the same experimental setup, as indicate in Fig. 12.

In order to perform both self-diffraction and P-scan measurements, as described at the end of Section 5.1, we started by positioning the sample as indicated in Fig. 12, which would correspond to Fig. 11(a). However, in the case of the Ag samples, due to the refraction of light, it was impossible to obtain $\chi^{(3)}_{3333}$ according to Fig. 11(c). Then, the measurements were performed for normal incidence and incidence at 45°. In the first case, it corresponds to Fig. 11(a) (normal incidence, vertical in Tables 3 and 4). In the second case (45°), the signal was measured for two positions, one such that the substrate containing the Ag nanocomposites was rotated 45° as indicated by the superior arrow in Fig. 12, but the incident optical polarization was kept parallel to the major axis of the nanoparticle (45° incidence, vertical in Tables 3 and 4, corresponding to Fig. 11(c)), addressing mainly $\chi^{(3)}_{3333}$. The other measurement was done in a similar way, but the incident optical polarization was kept parallel to the minor axis (45°, horizontal in Tables 3 and 4, substituting what it had been described for Fig. 11(b)), mainly related to $\chi^{(3)}_{1111}$. This has been achieved by rotating the sample 45° with respect to the axis normal to the setup, taking the first measurement and then, rotating the sample around its normal by 180°, measuring again.

5.3 Nonlinear optical results

According to what has been shown above and to our previous results (Oliver et al, 2006; Rodríguez-Iglesias, et al; Reyes-Esqueda et al, 2008), the nanocomposites thus fabricated show uniaxial symmetry. However, although the metallic anisotropic nanoparticles are all oriented in the same direction, as shown in Figs. 1 and 2, they do not exhibit polar order since they do not possess intrinsic dipolar moment. In consequence, as it has been shown in section 5.1, for nonlinear optical measurements using a fully degenerate setup, *i.e.* for $\chi^{(3)}(-\omega;\omega,\omega,-\omega)$, that the tensor has only three independent nonzero components: $\chi^{(3)}_{1111}$, $\chi^{(3)}_{1133}$ and $\chi^{(3)}_{3333}$. By following Fig. 11 and its discussion, we can perform the necessary

measurements to obtain these three elements, show the anisotropy of the nonlinear optical properties of the nanocomposites, and therefore their usefulness for straightforward nonlinear applications, as we have already shown for linear optical properties (Oliver et al, 2006; Reyes-Esqueda et al, 2008). Then, we measured the P-scan transmitted and the scalar self-diffracted intensities while varying the angular position of the nanocomposites according to Fig. 11, for a fixed polarization of the incident beams. First, we measured the single beam optical transmittance in order to obtain the nonlinear optical absorption coefficient for each position of the sample. The fitting was made considering that absorption is described by the expression $\alpha=\alpha_0+\beta I$; where α_0 and β represent the linear, and nonlinear absorption coefficients, respectively; and I is the incident intensity. Then, the self-diffraction experiments were performed and the transmitted and self-diffracted intensities were measured for each case.

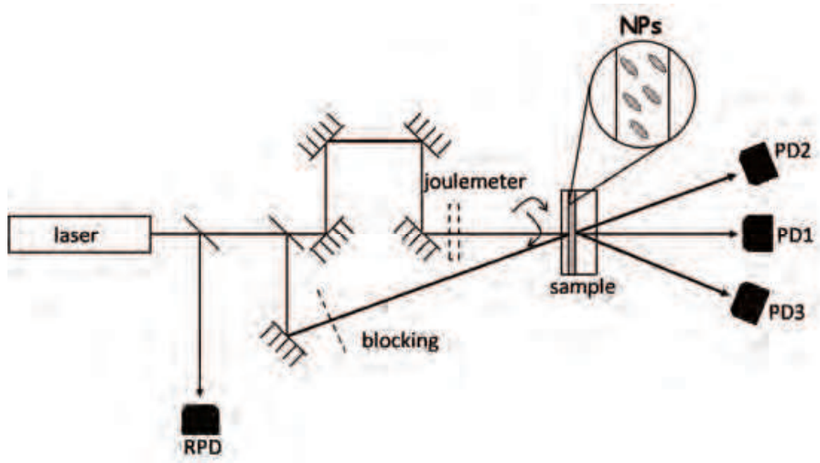

Fig. 12. Experimental setup used for self-diffraction and P-scan measurements (dashed components).

For the evaluation of the corresponding $|\chi^{(3)}_{eff}|$ value, we considered that nonlinear absorption takes place during the self-diffraction experiments. Thus, the numerical fitting was made by following the analysis of degenerate two-wave mixing with self-diffraction in the stationary regime for a thin nonlinear medium (Sánchez, 1992), but taking into account the results obtained for the nonlinear absorption for each case.

The $|\chi^{(3)}_{eff}|$, $\mathrm{Re}(\chi^{(3)}_{eff})$, and $\mathrm{Im}(\chi^{(3)}_{eff})$ values obtained for each sample, for each angular position, according to what has been described in Section 5.2, are shown in Tables 3 and 4. It is worth remarking that the self-diffraction and the P-scan signals were measured also for isotropic metallic nanocomposites, i.e. spherical-like Ag nanoparticles not deformed with Si, for each angular position as mentioned before, finding practically the same value for the nonlinear response.

Si fluence (×10^{15} ions/cm^2)	$\left\|\chi^{(3)}_{eff}\right\|$ normal incidence, vertical	$\left\|\chi^{(3)}_{eff}\right\|$ 45° incidence, vertical	$\left\|\chi^{(3)}_{eff}\right\|$ 45° incidence, horizontal
0.0		2.77	
0.5	2.73	3.42	1.46
0.8	2.29	3.09	1.80
1.0	2.28	3.26	1.33
2.0	1.99	2.12	1.44
5.0	3.36	2.79	2.05

Table 3. $|\chi^{(3)}_{eff}|$ *(×10^{-9} esu)* measurement for each angular position, Ag nanocomposites (*4.7×10^{16} ions/cm^2*), $\Delta|\chi^{(3)}_{eff}| = \pm 10^{-11}$ *esu* .

From Table 3, the difference in the measured values for the anisotropic nanocomposites, for each position, is quite clear. Therefore, from the given association of them to the different components of the nanocomposite third-order susceptibility tensor $\chi^{(3)}$, *i.e.*, the vertical measurements are associated to the major axis component $\chi^{(3)}_{3333}$, while the horizontal ones to the minor axis component $\chi^{(3)}_{1111}$; for similar geometric parameters of the nanocomposites, we can establish the inequality $|\chi^{(3)}_{eff}|_{\text{minor axis}} < |\chi^{(3)}_{eff}|_{\text{isotropic}} < |\chi^{(3)}_{eff}|_{\text{major axis}}$. These results are valid considering that the magnitude of the nonlinear optical response seems to be strongly dependent on the size and shape of the particles (López-Suárez et al, 2009), and our deformation technique for obtaining nanoellipsoids is a direct way of modifying both. One obvious implication that we can sort out from this result, is that the smaller the nanoparticle that 'sees' the incident light, the smaller the third order nonlinear optical response. This could be related to the near-field enhancement associated with the shape of the nanoparticle, indicating that the largest enhancement is obtained for the major axis, as has been shown for Au nanorods (Chau *et al*, 2009).

From Table 4, the anisotropy of the nonlinear absorption and refraction is quite clear for these anisotropic nanocomposites. Furthermore, $\mathrm{Re}(\chi^{(3)}_{eff})$, is positive for Ag indicating a self-focusing response. On the contrary, the imaginary part is negative for both axes, although the anisotropy is quite clear when comparing the measurements related to the minor and the major axes (the last two columns of Table 4). It has been previously indicated that there are different contribution to the nonlinear response for different pulse durations, since hot electrons, or even thermal effects, can take place besides the electronic response of the material (Torres-Torres *et al*, 2008a; Torres-Torres *et al*, 2009; Torres-Torres *et al*, 2008c). In this case, if we compare the femtosecond and picosecond results, it is possible to observe that the magnitude of the absorptive nonlinearity in anisotropic Ag nanoparticles is approximately two orders of magnitude stronger for the femtosecond regime. We assume that the density of particles in the sample and the lifetime associated with the optical excitation in the absorption process cannot be fast enough to allow the linear optical interactions to take place. Apparently, optical saturation is more easily induced for femtosecond irradiation, even when similar mechanisms of nonlinear optical absorption are exhibited in both regimes. This behavior related with the temporal response and changes in the absorptive nonlinearity mechanisms have been previously studied in other nanostructured materials (López-Suárez *et al*, 2009). On the other hand, an important consequence that can be derived from the changes in the absorptive nonlinearities in the different temporal regimes is that the nonlinear refractive index is strongly stimulated with picoseconds pulses, while for the femtosecond experiments

we do not obtain a significant refractive nonlinearity. We estimate that with the picosecond irradiation, strong intraband and interband transitions may take place according to the resonance of the major and the minor axis of the nanoparticle, respectively. As a result, changes in the magnitude of the real part of the third order nonlinearity are observed for picoseconds experiments as shown in Table 4.

Si fluence ($\times 10^{15}$ ions/cm^2)	normal incidence, vertical	45° incidence, vertical	45° incidence, horizontal
0.0		-3.5, 1.89	
0.5	-3.5, 1.84	-2.4, 2.34	-0.3, 1.00
0.8	-3.5, 1.56	-3.5, 2.12	-3.5, 1.22
1.0	-3.5, 1.56	-2.8, 2.23	-3.5, 0.89
2.0	-1.4, 1.34	-3.8, 1.45	-1.0, 1.00
5.0	-6.6, 2.28	-7.0, 1.89	-3.5, 1.39

Table 4. Im($\chi^{(3)}_{eff}$) *(×10^{-12} esu)*, and Re($\chi^{(3)}_{eff}$) *(×10^{-9} esu)* measurement for each angular position, Ag nanocomposites (*4.7×10^{16} ions/cm^2*).

6. Conclusions

We have shown a novel technique for producing composite materials containing deformed metallic nanoparticles that are placed at random but aligned in a given direction. This is achieved by a double ion-implantation technique; the first implantation produces the nanoparticles, while the second elongates them in a given direction. The resulting composite material has polarization dependent absorption spectra, due to a split of the surface plasmon resonance into two bands. Because of the alignment of the particles in a preferential direction, the material also presents strong birefringence, which has been characterized by a relatively simple ellipsometric technique.

We have also studied the nonlinear optical properties of these highly anisotropic nanocomposites in the femtosecond and picosecond regimes. In the femtosecond regime we find a mainly absorptive nonlinearity for wavelengths close to the surface plasmon resonance for polarization parallel to the long axis of the nanoparticles. The nonlinearity, studied using the z-scan technique, was found to consist of saturable absorption which was also polarization dependent, and this dependence was fitted reasonably well by a simple two-level model for anisotropic particles.

In the picosecond regime, the resonant nonlinear response was studied using the self-diffraction and 'P-scan' techniques. In this case the anisotropy of the nonlinear response was used to determine the different tensorial elements of $\chi^{(3)}_{ijkl}$, and to resolve the absorptive and refractive contributions to the nonlinearity. For these experiments, although significant nonlinear absorption was observed, the nonlinear response was shown to be dominated by nonlinear refraction, which was attributed to strong intra- and inter-band transitions induced by the resonant radiation.

The capability of tailoring their linear and nonlinear optical properties by the precise control of particle size, density, shape, and alignment, achievable with the implantation technique shown, makes these aligned nanostructured materials very interesting for applications in

all-optical switching devices, which exploit their nonlinearities, and possibly for the emerging field of plasmonic circuits.

7. References

Banerjee, P.P.; Danileiko, A.Y.; Hudson, T. & McMillen, D. (1998). P-scan analysis of inhomogeneously induced optical nonlinearities. *J. Opt. Soc. Am. B* 15, 2446-2454.

Barnes, W.L.; Dereux, A.; and Ebbessen, T.W. (2003). Surface plasmon subwavelength optics, *Nature* 424, 824-830.

Boyd, R.W. (1992) *Nonlinear Optics*, Academic Press, San Diego, chapter 4.

Cheang-Wong, J.C.; Morales, U.; Oliver, A.; Rodríguez-Fernández, L. & Rickards, J. (2006). MeV ion beam deformation of colloidal silica particles. *Nuclear Instruments and Methods in Physical Research B* 242, 452-454.

Davis, R. P.; Moad, A.J.; Goeken, G.S.; Wampler, R.D. & Simpson, G.J. (2008). Selection rules and symmetry relations for four-wave mixing measurements of uniaxial assemblies. *J. Phys. Chem. B* 112, 5834-5848.

Eisaman, M. D.; André, A.; Massou, F.; Fleischhauer, M.; Zibrov, A. S. & Lukin, A.S. (2005). Electromagnetically induced transparency with tunable single-photon pulses. *Nature* 438, 837-841.

Elim, H.I.; Yang, J.; Lee, J.Y.; Mi, J. & Ji, W. (2006). Observation of saturable and reverse-saturable absorption at longitudinal surface plasmon resonance in gold nanorods, *Applied Physics Letters* 88, 083107.

Genereux, F.; Leonard, S.W.; van Driel, H. M.; Birner, A. & Gösele, U. (2001). Large birefringence in two dimensional silicon photonic crystals. *Phys. Rev. B* 63, 161101(R).

Gonzalez, A. L.; Reyes-Esqueda, J.A. & Noguez, C. (2008). Optical properties of elongated noble metal nanoparticles, *J. Phys. Chem C* 112, 7356-7362

Hasui, K.; Grossman, D.G.; Mann, L.G.; Takahashi, H. & Borrelli, N.F. (2000). A high performance dichroic glass polarizer with a thickness of 15-35 μm. *Jpn. J. Appl. Phys.* 39, 1494-1496.

Hoa, X. D.; Kirk, A.G. & Tabrizian, M. (2007). Towards integrated and sensitive surface plasmon resonance biosensors: a review of recent progress. *Biosens. Bioelectron.* 23, 151-160.

Inouye, H.; Tanaka, K.; Tanahashi, I.; Hattori, T.; Nakatsuka H., (2000). Ultrafast Optical Switching in a Silver Nanoparticle System, *Japanese Journal of Applied Physics* 39, 5132-5133 (2000).

Johnson, N.F. & Christy, R.W. (1972). Optical constants of the noble metals. *Phys. Rev. B* 6, 4370-4379.

Kasai, H.; Nalwa, H.S.; Oikawa, H.; Okada, S.; Minami, S.; Kakuta A.; Ono, K.; Mukoh A. & Nakanishi, H. (1992) . *Japanese Journal of Applied Physics* 31, L1132.

Künzner, N.; Kovalev, D.; Diener, J.; Gross, E.; Timoshenko, V. Yu.; Polisski, G.; Koch, F. & Fujii, F. (2001). Giant birefringence in anisotropically nanostructured silicon. *Opt. Lett.* 26, 1265-1267.

Kyoung, M. & Lee, M. (1999). Nonlinear absorption and refractive index measurements of silver nanorods by the Z-scan thecnique, *Optics Communications* 171, 145-148.

Lamarre, J.M.; Billard, F.; Kerboua, C.H.; Lequime, M.; Roorda, S. & Martinus, L. (2008). Anisotropic nonlinear absorption of gold nanorods in a silica matrix. *Opt. Commun.* 281, 331-340.

Lopez-Suarez, A.; Torres-Torres, C.; R. Rangel-Rojo, Reyes-Esqueda, J.A.; Santana, G.; Ortíz, A.; Alonso, J.C. & Oliver, A. (2009). Modification of the nonlinear optical absorption and optical Kerr response exhibited by nc-Si embedded in a silicon-nitride film. *Opt. Express* 17, 10056-10068

Maier, S.A.; Kik, P.G.; Atwater, H.A.; Meltzer, S.; Harel, E.; Koel, B.E. & Requicha, A.A.G. (2003). Local detection of electromagnetic energy transport below the diffraction limit in metal nanoparticle plasmon waveguides. *Nature Materials* 2, 229-232.

Matsuda, S.; Yasuda, Y. & Ando, S. (2005). Fabrication of polyimide-blend thin films containing uniformly oriented silver nanorods and their use as flexible, linear polarizers. *Adv. Mater.* 17, 2221-2224.

Muskens, O.L.; Borgström, M.T.; Bakkers, E.P.A.M. & Gómez-Rivas, J. (2006). Giant optical birefringence in ensembles of semiconductor nanowires. *Appl. Phys. Lett.* 89, 233117.

Noguez, C. (2007). Surface plasmons on metal nanoparticles: the influence of shape and physical environment. *J.Phys. Chem. C.* 111, 3806-3819.

Oliver, A.; Reyes-Esqueda, J.A.; Cheang-Wong, J.C.; Román-Velázquez, C.E.; Crespo-Sosa A.; Rodríguez-Fernández, L.; Seman, J.A.; & Noguez, C. (2006). Controlled anisotropic deformation of Ag nanoparticles by Si ion irradiation. *Phys. Rev. B* 74, 245425.

Pérez-Juste, J.; Pastoriza-Santos, I.; Liz-Marzán, L. M. & Mulvaney, P. (2005). Gold nanorods: synthesis, characterization and applications. *Coordin. Chem. Rev.* 249, 1870-1901

Rangel-Rojo, R.; Kar, A.K.; Wherrett, B.S.; Carroll, M.; Cross, G.H.; & Bloor, D. (1995). Third-order optical nonlinearities of a polymeric film doped with a novel zwitterion, DEMI-3CNQ, *Rev. Mex. Fis.* 41, 832--840

Rangel-Rojo, R.; Yamada, S.; Matsuda, H.; Kasai, H.; Nakanishi, H.; Kar, A.K. & Wherrett, B.S. (1998). Spectrally resolved third-order nonlinearities in polydiacetylene microcrystals: influence of particle size, *J. Opt. Soc. Am. B* 15, 2937-2945

Rangel-Rojo, R.; McCarthy, J.; Bookey, H.T.; Kar, A.K.; Rodriguez-Fernandez, L.; Cheang-Wong, J.C.; Crespo-Sosa, A.; Lopez-Suarez, A.; Oliver, A.; Rodriguez-Iglesias, V. ; Silva-Pereyra, H. (2009). Anisotropy in the nonlinear absorption of elongated silver nanoparticles in silica, probed by femtosecond pulses. *Optics Communications* 282, 1909-1912.

Reyes-Esqueda, J.A.; Torres-Torres, C.; Cheang-Wong, J.C.; Crespo-Sosa, A.; Rodríguez-Fernández, L.; Noguez, C. & Oliver, A. (2008). Large optical birefringence by anisotropic silver nanocomposites, *Opt. Express* 16, 710-717.

Reyes-Esqueda, J.A.; Rodríguez-Iglesias, V.; Silva-Pereyra, H.G.; Torres-Torres, C.; Santiago-Ramírez, A.L.; Cheang-Wong, J.C.; Crespo-Sosa, A.; Rodriguez-Fernandez, L.; Lopez-Suarez, A. & Oliver, A. (2009). Anisotropic linear and nonlinear optical properties from anisotropy-controlled metallic nanocomposites. *Opt. Express* 17, 12849-12868.

Rodríguez-Iglesias, V.; Silva-Pereyra, H.G.; Cheang-Wong, J.C.; Reyes-Esqueda, J.A.; Rodríguez-Fernández, L.; Crespo-Sosa, A.; Kellerman, G. & Oliver, A. (2008). MeV Si ion irradiation effects on the optical absorption properties of metallic nanoparticles embedded in silica. *Nucl. Instrum. Methods B* 266, 3138-3142

Rodríguez-Iglesias, V.; Silva-Pereyra, H.G.; Torres-Torres, C.; Reyes-Esqueda, J.A.; Cheang-Wong, J.C.; Crespo-Sosa, A.; Rodriguez-Fernandez, L.; Lopez-Suarez, A. & Oliver, A. (2009). Large and anisotropic third-order nonlinear optical response from anisotropy-controlled metallic nanocomposites. *Opt. Commun.* 282, 4157-4161

Ruda, H.E. & Shik A. (2007). Nonlinear optical phenomena in nanowires. *Journal of Applied Physics* 101, 034312.

Saleh, B.E.A. & Teich, M.C. (1991). *Fundamental of Photonics*. Wiley-Interscience, John Wiley & sons, Inc. This equation differs from to the usual one in the reference because our analysis considers the angle between the wavevector and the normal to the particle, and not with its optical axis as it is usual. Anyway, both angles are related since their sum gives $\pi/2$, which explains the difference in this equation.

Sanchez, F. (1992). Two-wave mixing in thin nonlinear local-response media: a simple theoretical model. *J. Opt. Soc. Am. B* 9, 2196-2205

Seward III, T. P. (1974). Elongation and spheroidization of phase-separated particles in glass. *J. Non-Crystalline Solids* 15, 487-504.

Sutherland, R.L. (1996). Handbook of Nonlinear Optics. Marcel Dekker Inc, New York,.

Torres-Torres, C.; Reyes-Esqueda, J.A.; Cheang-Wong, J.C.; Crespo-Sosa, A.; Rodríguez-Fernández, L. & Oliver, A. (2008a). Optical third order nonlinearity by nanosecond and picosecond pulses in Cu nanoparticles in ion-implanted silica. Journal of Applied Physics, 104, 014306 1-0143065.

Torres-Torres, C.; Khomenko, A.V.; Tamayo-Rivera, L.; Rangel-Rojo, R.; Mao, Y. & Watson, W. H. (2008b). Measurements of nonlinear optical refraction and absorption in an amino-triazole push-pull derivative by a vectorial self-diffraction method. *Opt. Commun.* 281 3369–3374.

Torres-Torres, C.; Lopez-Suarez, A.; Tamayo-Rivera, L.; Rangel-Rojo, R.; Crespo-Sosa, A.; Alonso, J.C. & Oliver, A. (2008c). Thermo-optic effect ant third order nonlinearity in nc-Si embedded in a silicon nitride film. *Opt. Express* 16, 18390-18396.

Torres-Torres, C.; Trejo-Valdez, M.; Sobral, H.; Santiago-Jacinto, P. & Reyes-Esqueda, J.A. (2009). Stimulated emission and optical third order nonlinearity in Li-doped nanorods. *J. Phys. Chem C* 113, 13515-13521

Yildirim, H. & Bulutay, C. (2008). Enhancement of optical switching parameter and third-order optical nonlinearities in embedded Si nanocrystals: a theoretical assessment. *Optics Communications* 281, 4118-4120.

IntechOpen

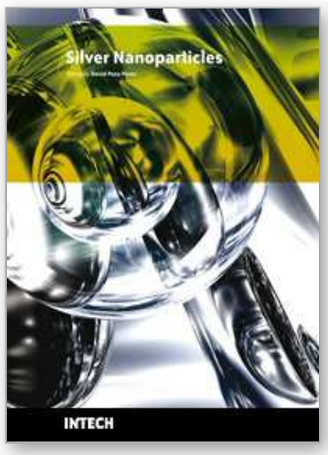

Silver Nanoparticles

Edited by David Pozo Perez

ISBN 978-953-307-028-5
Hard cover, 334 pages
Publisher InTech
Published online 01, March, 2010
Published in print edition March, 2010

Nanotechnology will be soon required in most engineering and science curricula. It cannot be questioned that cutting-edge applications based on nanoscience are having a considerable impact in nearly all fields of research, from basic to more problem-solving scientific enterprises. In this sense, books like “Silver Nanoparticles” aim at filling the gaps for comprehensive information to help both newcomers and experts, in a particular fast-growing area of research. Besides, one of the key features of this book is that it could serve both academia and industry. “Silver nanoparticles” is a collection of eighteen chapters written by experts in their respective fields. These reviews are representative of the current research areas within silver nanoparticle nanoscience and nanotechnology.

InTech Europe
University Campus STeP Ri
Slavka Krautzeka 83/A
51000 Rijeka, Croatia
Phone: +385 (51) 770 447
Fax: +385 (51) 686 166
www.intechopen.com

InTech China
Unit 405, Office Block, Hotel Equatorial Shanghai
No.65, Yan An Road (West), Shanghai, 200040, China
中国上海市延安西路65号上海国际贵都大饭店办公楼405单元
Phone: +86-21-62489820
Fax: +86-21-62489821

IntechOpen